Investigation of flow phenomena in air–water safety relief valves by means of a discontinuous Galerkin solver

F. Bassi [a], A. Crivellini [b], V. Dossena [c], N. Franchina [a,*], M. Savini [a]

[a] *Università degli Studi di Bergamo, Dipartimento di Ingegneria, Italy*
[b] *Università Politecnica delle Marche, Dipartimento di Ingegneria Industriale e Scienze Matematiche, Italy*
[c] *Politecnico di Milano, Dipartimento di Energia, Lab. di Fluidodinamica delle Macchine, Italy*

Article history:
Received 8 March 2013
Received in revised form 18 September 2013
Accepted 18 November 2013
Available online 28 November 2013

1. Introduction

Safety relief valves are devices widely used to protect industrial equipments from possible failures caused by unexpected off-design overpressure. The most relevant characteristic of the device is the capability of exhausting a prescribed amount of fluid at a specific overpressure and closing again within a narrow pressure range.

In some cases they are required to perform properly both for compressible and incompressible flows, *e.g.* in shell-type water–gas heat exchangers and/or in the economizer section of steam boilers where liquid or vapor can be contained, depending on the plant operating condition. It is at first glance evident that the behavior could be significantly different. At fixed opening position, for liquids the mass flow rate is mainly driven by the pressure difference acting between the inlet and outlet flange, whilst for gases is driven by the ratio of inlet to outlet absolute pressure and by the shape and position of the sonic throat (if the overall expansion ratio is sufficiently higher than the critical one). Moreover, at the same pressure, the disc lift is supposed to vary owing to the different fluid dynamic forces acting against the spring load resulting from the different pressure distribution on the moving device surface.

The operating and flow characteristics of a size range of safety valves are assessed by performing several experimental tests at different pressures on different valve bodies extracted from the size range subject to performance certification. The goal of the test procedure is to verify the ability of the safety valve designer because every tested sample should provide the same discharge coefficient (within a prescribed small tolerance), independently of pressure and size, and guarantee opening and reclosing within strict tolerances. Note that in the testing procedure, the Mach and Reynolds numbers, but also some geometric ratios (*e.g.* the inlet and outlet flanges commercially adopted may not follow in similitude the valve body) may vary. In the case of valves working with either compressible or incompressible fluids, two different discharge coefficients can be prescribed for the same valve size

* Corresponding author. Tel.: +39 0352052020; fax: +39 0352052077.
E-mail address: nicoletta.franchina@unibg.it (N. Franchina).

Nomenclature

F	dimensional thrust
K	discharge coefficient
P_g	gauge pressure
Q	mass flow rate
$T_{nd} = F/(P_g A)$	non-dimensional thrust
a	sonic speed
$v_{id} = \sqrt{2P_g/\rho}$	ideal velocity
A	orifice area
exp	experimental

Greek symbols

β	total to static expansion ratio
γ	specific heat ratio
ρ	density

Subscripts

c	minimum flow area
T	total
1	orifice entrance
2	exit flange

range. However, in either case the flow characteristics of the valves in the given size range should be constant. The task for the designer then is a challenging one and CFD simulations are very helpful in the development stages before the final experimental certification. Laboratory tests can be performed only in few facilities and, besides their cost, could be unfeasible with certain gases and/or for large sizes, as API 526 T-type orifices.

The authors have already carried out numerical and experimental investigations [1–4] aimed at clarifying the physical reasons for the observed performance of safety relief valves in several working conditions, and the present work is a further step toward a better understanding of the devices behavior. For this purpose, the paper presents high-order accurate Discontinuous Galerkin (DG) solutions of compressible (air) and incompressible (water) flows on a 2″ J 3″ safety relief valve and comparison with measurements performed at the Politecnico di Milano safety valves test rig. Both experimental and computational results are analyzed and compared in order to investigate the different trend of both the discharge coefficient and the thrust acting on moving device as function of the increasing upstream pressure at fixed geometry (*i.e.* at fixed disc lift).

The DG solver employed solves the Reynolds averaged Navier–Stokes (RANS) equations coupled with a k–ω turbulence model. The polynomial approximation is defined in the physical space and is continuous within each element and discontinuous at element interfaces. For steady problems, a linearly implicit backward Euler method with an analytically derived Jacobian matrix of the residuals is used. For compressible flows, numerical inviscid and viscous fluxes at element interfaces are computed by means of the "exact" Riemann solver of Gottlieb and Groth [5] and of the BRMPS scheme [6], respectively. Further details about the DG implementation for the compressible RANS and k–ω turbulence model equations can be found in [7].

Across discontinuities, like shock waves and slip lines occurring inside safety valves at transonic and supersonic regimes, high-order solutions need additional dissipation to control the numerical oscillations arising within the mesh elements. For this purpose, the shock-capturing technique described in [2] is used. The technique is local and introduces an amount of artificial viscosity proportional to the inviscid residual of the DG space discretization that allows crisp representations of discontinuities and preserves high accuracy within smooth regions. For incompressible flows, the DG solver handles the incompressible RANS and k–ω equations using the original formulation of the numerical inviscid flux presented in [8,9], and again the BRMPS scheme [6] for the discretization of the viscous flux.

The purpose of this paper is threefold. First, it presents an analysis and discussion on the observed trends of global characteristics, *i.e.* the opening force and the discharge coefficient, obtained in an experimental campaign performed both in air and water on a valve designed for steam–water double protection. Second, these results are used to assess the reliability and accuracy of the high-order DG code here employed. Third and most important, the paper shows that a detailed knowledge of the flow field in the inner valve body, almost impossible to be measured but quite easily obtained from numerical simulations, provides physical insight into the flow features that could be useful in the device design.

The outline of the paper is as follows. Section 2 describes the main feature of the DG solver applied to incompressible fluids. Numerical results are discussed and compared with experimental data in Section 3. Finally, Section 4 gives some concluding remarks on the different operational behavior of valves working with water or air.

2. The DG solver for turbulent incompressible flows

In this section the main features of the DG solver for the incompressible RANS equations coupled with a k–ω turbulence model are described. The approach follows from a quite natural extension of the DG implementation used for the compressible flow simulations [7,2], to the incompressible Navier–Stokes solver introduced in [8,9]. The new solver has already been extensively tested and a more comprehensive presentation of the method will be given in a forthcoming paper, now in preparation.

The RANS and k–ω turbulence model equations for an incompressible flow with uniform density and constant transport properties can be written as

$$\frac{\partial u_j}{\partial x_j} = 0, \tag{1}$$

$$\frac{\partial u_i}{\partial t} + \frac{\partial}{\partial x_j}(u_j u_i) = -\frac{\partial p}{\partial x_i} + \frac{\partial \hat{\tau}_{ji}}{\partial x_j}, \tag{2}$$

$$\frac{\partial k}{\partial t} + \frac{\partial}{\partial x_j}(u_j k) = \frac{\partial}{\partial x_j}\left[(\nu + \sigma^* \bar{\nu}_t)\frac{\partial k}{\partial x_j}\right] + \tau_{ij}\frac{\partial u_i}{\partial x_j} - \beta^* \bar{k} e^{\tilde{\omega}_r}, \tag{3}$$

$$\frac{\partial \tilde{\omega}}{\partial t} + \frac{\partial}{\partial x_j}(u_j \tilde{\omega}) = \frac{\partial}{\partial x_j}\left[(\nu + \sigma \bar{\nu}_t)\frac{\partial \tilde{\omega}}{\partial x_j}\right] + \frac{\alpha}{\bar{k}}\tau_{ij}\frac{\partial u_i}{\partial x_j} - \beta e^{\tilde{\omega}_r} + (\nu + \sigma \bar{\nu}_t)\frac{\partial \tilde{\omega}}{\partial x_k}\frac{\partial \tilde{\omega}}{\partial x_k}, \tag{4}$$

where u_j is the j-component of the velocity vector, p is the pressure and $\hat{\tau}_{ji}$ is the j-component in i-direction of the total stress tensor. The turbulent and total stress tensors and the eddy viscosity are given by

$$\tau_{ij} = 2\bar{\nu}_t\left[S_{ij} - \frac{1}{3}\frac{\partial u_k}{\partial x_k}\delta_{ij}\right] - \frac{2}{3}\bar{k}\delta_{ij}, \tag{5}$$

$$\hat{\tau}_{ij} = 2\nu\left[S_{ij} - \frac{1}{3}\frac{\partial u_k}{\partial x_k}\delta_{ij}\right] + \tau_{ij}, \tag{6}$$

$$\bar{\nu}_t = \alpha^* \bar{k} e^{-\tilde{\omega}_r}, \quad \bar{k} = \max(0, k) \tag{7}$$

where

$$S_{ij} = \frac{1}{2}\left(\frac{\partial u_i}{\partial x_j} + \frac{\partial u_j}{\partial x_i}\right)$$

is the mean strain-rate tensor. The closure parameters α, α^*, β, β^*, σ, σ^* are those of the high-Reynolds number k–ω model of Wilcox [10]. The non-standard form of the above k–ω model has been introduced in [7] and employs the variable $\tilde{\omega} = \log \omega$ instead of ω in order to guarantee positivity and smoother near-wall distribution of ω. The limited value $\bar{k}$ and the related eddy viscosity $\bar{\nu}_t$, given by Eq. (7), are needed to deal with possible negative values that the solution of the turbulent kinetic energy can take during computations. Finally, in the source terms of Eqs. (3) and (4) and in the eddy viscosity defined by Eq. (7) the variable $\tilde{\omega}_r$ is employed in place of $\tilde{\omega}$ to guarantee that the turbulent stress tensor fulfills suitably defined "realizability" conditions entailing positive normal turbulent stresses and shear stresses satisfying the Schwartz inequality, see [11] for more details.

The system of Eqs. (1)–(4) can be written in the following compact form

$$\frac{\partial \mathbf{u}^0}{\partial t} + \nabla \cdot \boldsymbol{\mathcal{F}}(\mathbf{u}, \nabla \mathbf{u}) + \mathbf{s}(\mathbf{u}, \nabla \mathbf{u}) = \mathbf{0}, \tag{8}$$

where $\mathbf{u} \in \mathbb{R}^m$ defines the unknown solution vector of the m primitive variables $(p, u, v, w, k, \tilde{\omega})$, with $\mathbf{u}^0 = (0, u, v, w, k, \tilde{\omega})$. The vector $\boldsymbol{\mathcal{F}} \in \mathbb{R}^m \otimes \mathbb{R}^d$ is the sum of inviscid and viscous flux functions and $\mathbf{s} \in \mathbb{R}^m$ is the turbulent source term vector.

The discretization of Eq. (8) is defined on a set of non-overlapping elements of arbitrary shape defining the triangulation $\mathcal{T}_h = \{K\}$ of the physical domain Ω_h. On $\mathcal{T}_h$ each component of the solution vector is approximated using the following functional setting

$$u_{h_i} \in V_h \equiv \{v_h \in L^2(\Omega_h) : v_h|_K \in \mathbb{P}_k(K) \forall K \in \mathcal{T}_h\}, \tag{9}$$

where $\mathbb{P}_k(K)$ is the space of polynomials up to degree k continuous over each element $K \in \mathcal{T}_h$.

The DG discretization of Eq. (8) requires to find $u_{h_i} \in V_h, (i = 1, \ldots, m)$ such that

$$\begin{aligned}
&\sum_{K\in\mathcal{T}_h} \int_K v_{h_i} \frac{\partial u^0_{h_i}}{\partial t} \mathrm{d}\mathbf{x} - \sum_{K\in\mathcal{T}_h} \int_K \nabla_h v_{h_i} \cdot \boldsymbol{\mathcal{F}}_i(\mathbf{u}_h, \nabla_h \mathbf{u}_h + \mathbf{R}([\![\mathbf{u}_h]\!]))\mathrm{d}\mathbf{x} \\
&+ \sum_{f\in\mathcal{F}} \int_f [\![v_{h_i}]\!] \cdot \widehat{\boldsymbol{\mathcal{F}}}_i \left(\mathbf{u}_h^{\pm}, \left(\nabla_h \mathbf{u}_h + \eta_f \mathbf{r}_f [\![\mathbf{u}_h]\!] \right)^{\pm} \right) \mathrm{d}\sigma \\
&+ \sum_{K\in\mathcal{T}_h} \int_K v_{h_i} s_i(\mathbf{u}_h, \nabla_h \mathbf{u}_h + \mathbf{R}([\![\mathbf{u}_h]\!]))\mathrm{d}\mathbf{x} = 0,
\end{aligned} \tag{10}$$

for any arbitrary test function $v_{h_i} \in \mathbf{V}_h$. The jump operator $[\![\cdot]\!]$ is defined by

$$[\![\mathbf{u}_h]\!] \equiv \mathbf{u}_h^+ \mathbf{n}^+ + \mathbf{u}_h^- \mathbf{n}^-, \tag{11}$$

and $\pm$ superscripts denote the traces of the solution over an interface f shared by two adjacent elements K^+ and K^-, and $\mathcal{F}$ is the collection of all faces f.

The vector $\widehat{\boldsymbol{\mathcal{F}}}_i$ in Eq. (10) is the sum of the inviscid and viscous numerical fluxes that must be suitably defined to obtain a stable and consistent discretization. According to the approach described in [8,9], the inviscid numerical flux results from the solution of local Riemann problems at each integration point on the interfaces. The solution of such local 1D Riemann problems can be accomplished by relaxing the continuity constraint, *i.e.*, introducing an artificial compressibility-like perturbation in the continuity equation of the Riemann solver. The resulting exact Godunov Riemann solver allows coupling velocity and pressure jumps at element interfaces and provides an accurate and stable formulation of the inviscid numerical flux. As shown in [9], the Riemann solver can deal in a unified way with the advection of any other scalar quantity, such as the velocity components tangential to the interface or the turbulence model quantities.

According to the BRMPS discretization of the viscous fluxes [6], the gradients appearing in the fluxes of Eq. (10) are modified by adding the so-called lifting functions $\mathbf{R}$ and $\mathbf{r}_f$ to the gradients internal to the elements. These lifting functions are needed to ensure both the consistency and the stability of the scheme and account for the contribution of interface jumps of any quantity to its gradient within elements. Details on the BRMPS scheme can be found in [13].

2.1. Time integration

After space discretization, Eq. (10) can be written as

$$\mathbf{I}^0 \frac{\mathrm{d}\mathbf{U}}{\mathrm{d}t} + \mathbf{R}(\mathbf{U}) = \mathbf{0}, \tag{12}$$

where $\mathbf{U}$ is the global vector of unknown degrees of freedom, $\mathbf{R}$ the residuals vector and $\mathbf{I}^0$ the identity matrix with zero entries in the positions corresponding to the pressure degrees of freedom. Eq. (12) defines a system of non-linear differential algebraic equations (DAEs) which has been integrated in time by means of the linearly implicit Euler method that at each time step requires solving the linear system

$$\left(\frac{\mathbf{I}^0}{\Delta t} + \frac{\partial \mathbf{R}}{\partial \mathbf{U}}\bigg|^n \right) \left(\mathbf{U}^{n+1} - \mathbf{U}^n \right) + \mathbf{R}(\mathbf{U}^n) = \mathbf{0}. \tag{13}$$

The Jacobian matrix of residuals has been computed analytically and fully accounts for the dependence of residuals on the unknown variables and derivatives, including the implicit treatment of lifting operators and of boundary conditions.

For the steady state computations presented in this work the pseudo-transient continuation strategy here used, based on local time stepping, follows the implementation described in [12].

The linear system corresponding to Eq. (12) is solved with the iterative preconditioned GMRES method using the PETSc library [14,15]. The code employs the METIS package [16] for grid partitioning and MPICH for the message passage communication required by data access on remote processors.

3. Numerical results

Numerical results are presented up to $\mathbb{P}_2$ solution for a 2″ J 3″ safety valve operating both with air and water at expansion ratios $\beta = \mathrm{P}_{T,1}/\mathrm{P}_2$ ranging from 1.5 to 6. Fig. 1 shows the computational domain, consisting of about 163,000 elements, with the height of the first cell off solid wall equal to 10^{-4} times the orifice radius (17.1 mm). Preliminary DG numerical computations allowed to coarsen the numerical domain up to this extent while preserving a resolution good enough to capture the fundamental physics of interest.

3.1. Computation at disc lift $h = 13$ mm

The DG solver has been first validated in water against experimental measurements at $P_g = 4.95$ bar, *i.e.* $\beta = 5.89$. The computed discharge coefficient and (dimensional) thrust for $\mathbb{P}_{0\to2}$ solutions are summarized in Table 1 and corresponding experimental data are reported in Table 2.

The mesh employed has been defined to obtain a triangulation with a viscous layer of the same resolution as the one adopted in the compressible case. Due to the reduced Reynolds number,

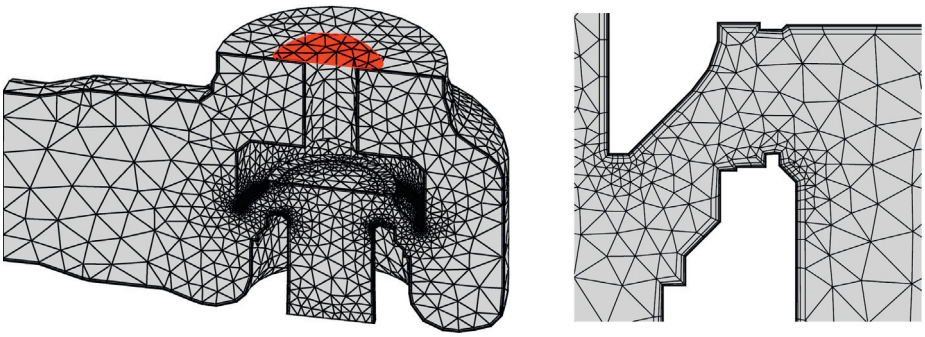

(a) Full grid (b) Detail of the symmetry plane

Fig. 1. Computational domain made of 163,000 elements.

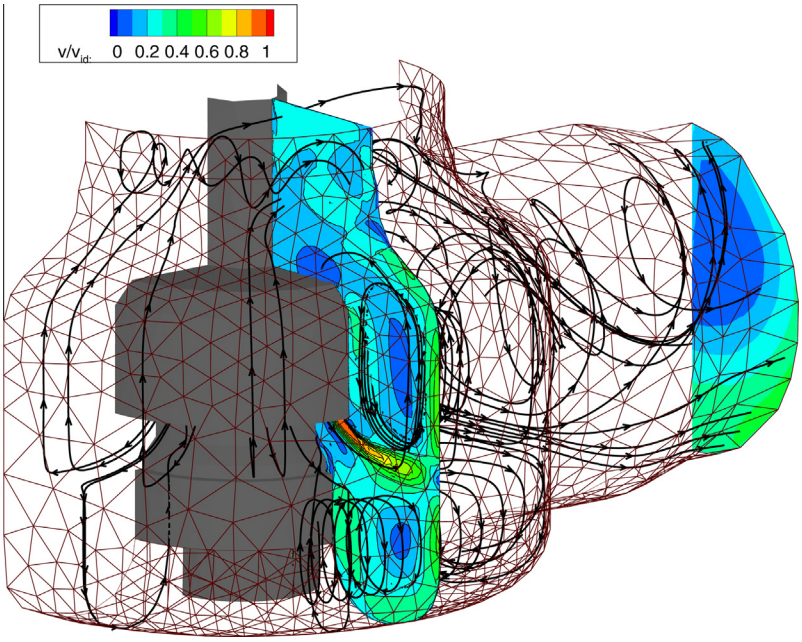

Fig. 2. Streamtraces and velocity contours of $\mathbb{P}_2$ solution of valve operating with water at $\beta = 6$.

Table 1
Discharge coefficient and net thrust of $\mathbb{P}_{0\to 2}$ computations of valve operating with water at $\beta = 5.89$, disc lift $h = 13$ mm.

$\mathbb{P}_k$	0	1	2
F[N]	719	1018	1093
K	0.820	0.772	0.742

Table 2
Experimental discharge coefficient and net thrust of valve operating with water, disc lift $h = 13$ mm.

β	3.97	4.94	5.89	6.98
P_g[bar]	3.00	3.99	4.95	6.05
F[N]	609	808	1011	1242
T_{nd}	2.23	2.23	2.24	2.26
K	0.759	0.756	0.761	0.760

which in water is about three times lower than in air, the mesh displayed in Fig. 1 has about half the number of elements. Despite the similar discretization, comparing the results with those of compressible simulations at lower lift (see [1]), one can notice a not negligible difference between $\mathbb{P}_1$ and $\mathbb{P}_2$ solutions, indicating grid/polynomial degree not fully converged solutions. Further work is needed to clarify this behavior. However, we believe that the level of accuracy of the results here presented already allows to adequately investigate the discharge capability of the safety relief device when working with water.

A close inspection at $\mathbb{P}_1$ versus $\mathbb{P}_2$ isovelocity contours (not shown here) reveals how the third-order solution better resolves the flow gradients in the critical region under the disc, limiting both the overspeed on the convex sides and the extent of the zone at minimum pressure. The resulting effect is a pressure increase (and a velocity decrease) on the lower disc surface. The discharged mass flow in transonic regime depends on the losses and on flow path only up to the throat, whereas in the incompressible case these two factors retain their importance downstream, as far as the exit section. From this observation, one can therefore conclude that in safety valves operating with liquids an accurate representation of viscous phenomena like boundary layer growth, detachment and separation, has the strongest influence.

It is important to highlight that in actual water valve testing the lowest possible pressure is limited by the occurrence of cavitation; on the contrary the solver includes, at present, no model of phase transition and therefore the computed pressure may exhibit

Table 3
Discharge coefficient and net thrust of $\mathbb{P}_{0\to 2}$ computations of valve operating with water at $\beta = 1.5$, disc lift h = 13 mm.

$\mathbb{P}_k$	0	1	2
F[N]	61	96	110
K	0.825	0.763	0.754

Table 4
Discharge coefficient and net thrust of $\mathbb{P}_1$ computation of valve operating with air at $\beta = 1.5$ and $\beta = 5.89$, disc lift h = 13 mm.

β	1.5	5.89
F[N]	100	888
K	0.863	0.969

negative values. Whether or not this could be a relevant point of discrepancy between experiments and simulations, the results here obtained and discussed well compare with measurements within an acceptable engineering tolerance. Moreover, a wide experimental campaign carried out to evidence the effects of cavitation on both thrust and discharge coefficient has been also performed at the LFM (Laboratorio di Fluidodinamica delle Macchine of Politecnico di Milano): tests performed with a constant pressure difference of 4 bar across the valve have shown no changes of the discharge coefficient and of the non-dimensional thrust (with the exception of the small influence of the constant atmospheric pressure contribution acting on the valve stem, as better clarified in the following) for absolute outlet pressure ranging from 0.5 bar to 5 bar. It is therefore possible to assume that cavitation is not affecting the valve performance in the operational range considered in the present paper.

Commenting Table 2, the constancy of K and of the thrust made non-dimensional by dividing it by the gauge pressure and orifice area can be observed. In all experiments in fact the resulting non-dimensional thrust is about 2.23. This fact suggests to check the behavior at very low expansion ratio and thus a case was run with $P_g = 0.507$ bar ($\beta = 1.5$), which represents the minimum value requiring the compliance with the European PED (Pressure Equipment Directive): its outcome is reported in Table 3. Again, the same comments previously done apply to K and F, the non-dimensional thrust being 2.06.

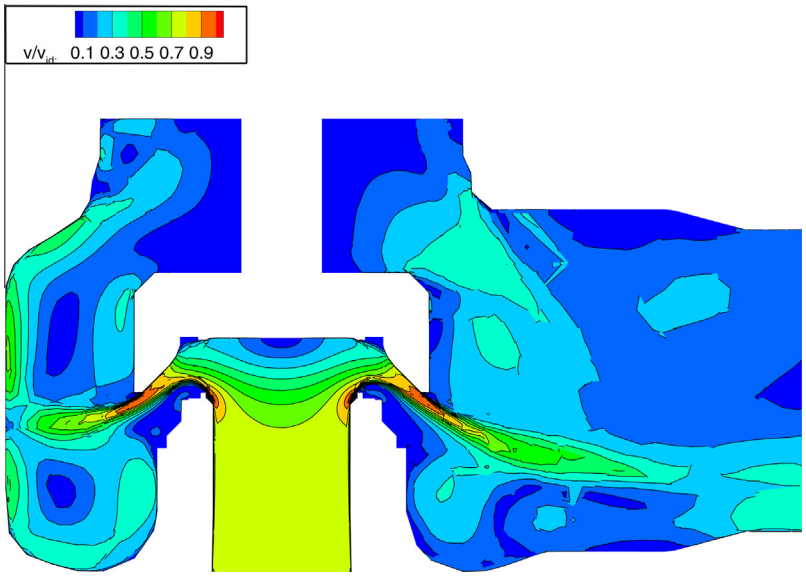

Fig. 3. $\mathbb{P}_2$ solution of valve operating with water at $\beta = 5.89$: non-dimensional velocity contours on the symmetry plane.

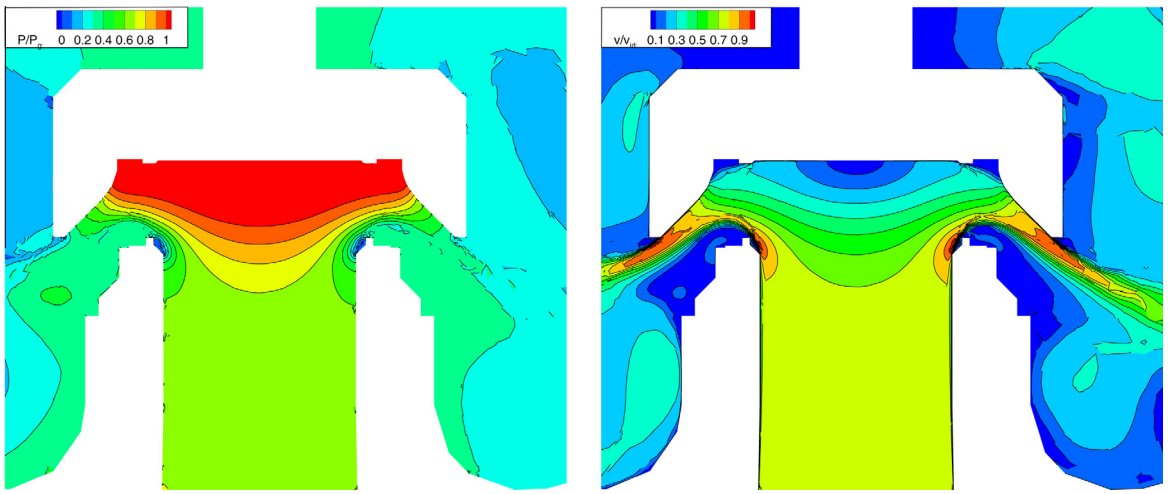

Fig. 4. $\mathbb{P}_2$ solution of valve operating with water at $\beta = 5.89$: detail of non-dimensional pressure and velocity contours on the symmetry plane.

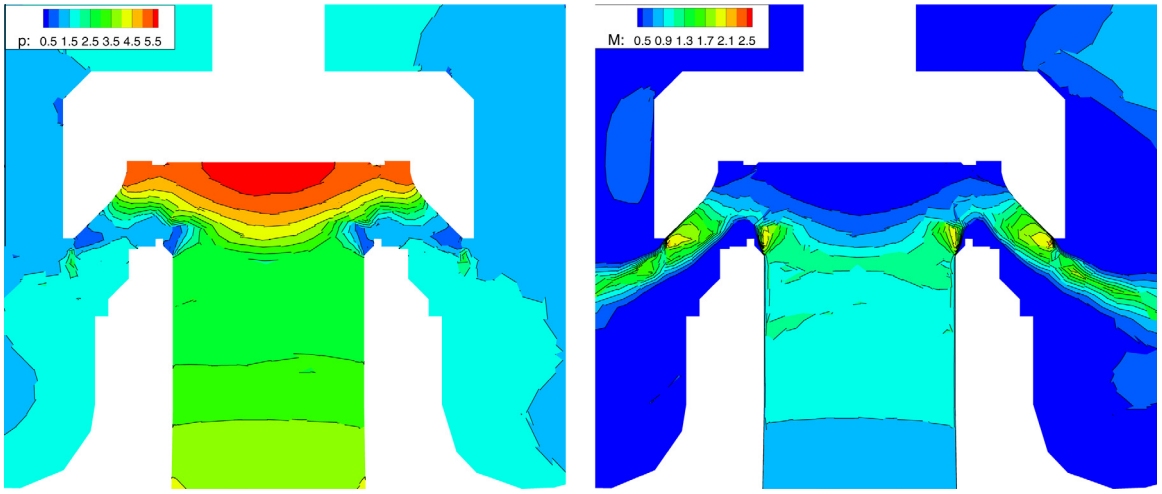

Fig. 5. $\mathbb{P}_1$ solution of valve operating with air at $\beta = 5.89$: detail of non-dimensional pressure and Mach number contours on the symmetry plane.

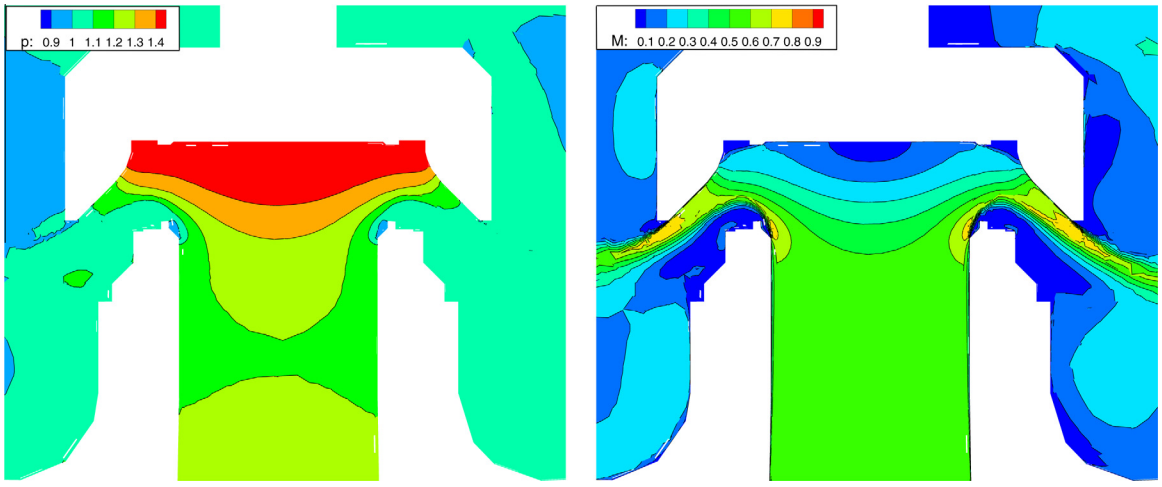

Fig. 6. $\mathbb{P}_2$ solution of valve operating with air at $\beta = 1.5$: detail of non-dimensional pressure and Mach number contours on the symmetry plane.

Figs. 3 and 4 illustrate the non-dimensional pressure and velocity contours; as it is customary in the representation of DG results, isolines are drawn without any sort of smoothing or interpolation procedure. Numerical solution at $\beta = 1.5$ shows that the pressure field scales almost perfectly with P_g while the velocity field with its square root; there is only a slight difference in non-dimensional force. This variation is due to the raising importance of the atmospheric pressure contribution when the upstream total pressure is lowered being the resulting force the sum of three terms: (1) the upward pushing force on the lower side of the disc, (2) the body backpressure acting on the upper side of the disc, (3) the ambient pressure acting on the stem rear upper surface (marked in bold-red[1] in Fig. 1). It is worth noting that if the discharge coefficient is nearly constant, the actual mass flow rate (and velocity field) scales with the square root of the upstream gauge total pressure and therefore, recalling what said above (net thrust proportional to P_g), with the square root of the net opening total force as well. As a consequence F is proportional to Q^2. Moreover, the discharge coefficient can also be viewed as the square root of the hydraulic efficiency and its constancy indicates that there is only one non-dimensional incompressible solution (*i.e.* the influence of Reynolds number is negligible). Fig. 2, which shows the flow streamtraces in the valve body and the velocity contours on the exit plane as well as on a plane passing through the axis of symmetry parallel to exit surface, gives an idea of the curly and complicated paths followed by fluid particles inside the safety device.

Then, the attention was focused on the behavior of the same safety valve operating in air. In [1] a complete validation of the compressible DG code is reported besides an exhaustive discussion on the compressible gas dynamic effects that will not be repeated here. In this case the greater lift (13.1 mm against 10 mm of the previous investigation reported in [1]) places the minimum flow section (sonic throat) just at the orifice entrance, a quite unusual working condition.

Global results of trials in air at the same lift and expansion ratios as in water testing (1.5 and approximately 6) are reported in Table 4; pressure and Mach number contours are illustrated in Figs. 5 and 6. As it is expected, in the transonic case the discharge coefficient is close to the unity whilst at very low expansion ratio it is about ten percent lower. This can be ascribed to the already mentioned influence of viscous losses throughout the whole valve flow path. Comparing the valve behavior in air and water, it is immediately evident the much higher value of K_{air}, even in the subsonic case. Beside the favorable compressibility effect on the local flow contraction coefficient (see again [1]), it must be also stressed

[1] For interpretation of color in Fig. 1, the reader is referred to the web version of this article.

that the Reynolds number is greater in air than water. Table 5 contains the reference Reynolds numbers based on the orifice radius, the dynamic viscosity, and the same quantities used in the definition of the ideal mass flow rate, *i.e.*

$$\rho v_{\mathrm{id}} = \sqrt{2\rho P_g}, \quad \rho_c a_c = \rho_T a_T \left[\left(\frac{\gamma+1}{2} \right)^{-\frac{\gamma+1}{2(\gamma-1)}} \right] \rightarrow \rho_T a_T \left[\beta^{-\frac{\gamma+1}{2\gamma}} \right]$$

in the case of water and of air (choked → unchoked), respectively. As one can see, when the valve is operating in water, the Reynolds number is about 2.5 times smaller than in air. In the authors'opinion, based on their own experience, the compressibility effect bears a stronger influence on K than the viscous one, apart from special situations involving for example a transitional boundary layer. Comparing the results shown in Tables 1 and 3 (admittedly with fully converged) with values of Table 4, one could anyway expect a higher total net force on the valve disc working with water. This effect appears to be stronger at higher expansion ratios, typical of safety relief valves operating with air.

Table 5
Reynolds number ($\cdot 10^5$) in water and air flows.

β	1.5	3	6
Re water	1.5	3	4.74
Re air	4.08	6.75	13.5

Table 6
Discharge coefficient and net thrust of DG $\mathbb{P}_1$ computation and experimental data of valve operating with air at $\beta = 1.5,\ 3$ and 6 at disc lift $h = 10$ mm.

β	1.5		3		6	
	DG	Exp	DG	Exp	DG	Exp
F[N]	93	94.25	379	359	978	970
K	0.816	0.81	0.924	0.899	0.931	0.904

3.2. Computation at disc lift $h = 10$ mm

The aim of the present investigation is to clarify the (possibly) different behavior of the same safety relief valve operating in air or water; in order not to draw hasty conclusions, other lift positions, *e.g.* $h = 10$ mm, should be used for completeness and comparison purpose. Table 6 contains the resulting global parameters, both computed and measured, when the valve operates in air at $\beta = 1.5, 3$, and 6 while Fig. 7 shows the pressure and Mach number contours on the symmetry plane, for the same cases.

Comparing this set of data with Table 4, one can observe how at lower lift the discharge coefficient always reduces whilst the opening force increases for $\beta = 6$ and decreases for $\beta = 1.5$. The cause of the apparently contradictory trends lies in the strong displacement of the throat position that, at the lower lift, moves from the orifice downstream toward the outer part of the disc lower surface, as evident from Figs. 5–7. The throat width is therefore reduced as well as the flow total pressure at its location; as a consequence K must decrease (the observed reduction of K is about 5 percent). On the other hand, the outer shift of the sonic throat pressurizes the lower part of the disc rising the net total thrust which increases more than 10%.

In the subsonic test case ($\beta = 1.5$) there is of course no such a pressurization and thus the resulting force increases with mass flow (and disc lift). The flow path at lower lift is more constrained and characterized by a smaller radius of curvature and channel hydraulic diameter, thus leading to greater flow contraction and viscous losses. These flow features result in a reduction of K and subsequently of the opening thrust.

When the valve is operating in water there are no transonic effects but only different flow paths and area variations. The most remarkable one is a sharper 90° bend under the disc when $h = 10$ mm as shown in Fig. 8, where the isovelocity contours of $\mathbb{P}_1$ solution are displayed. This last issue, with the related losses,

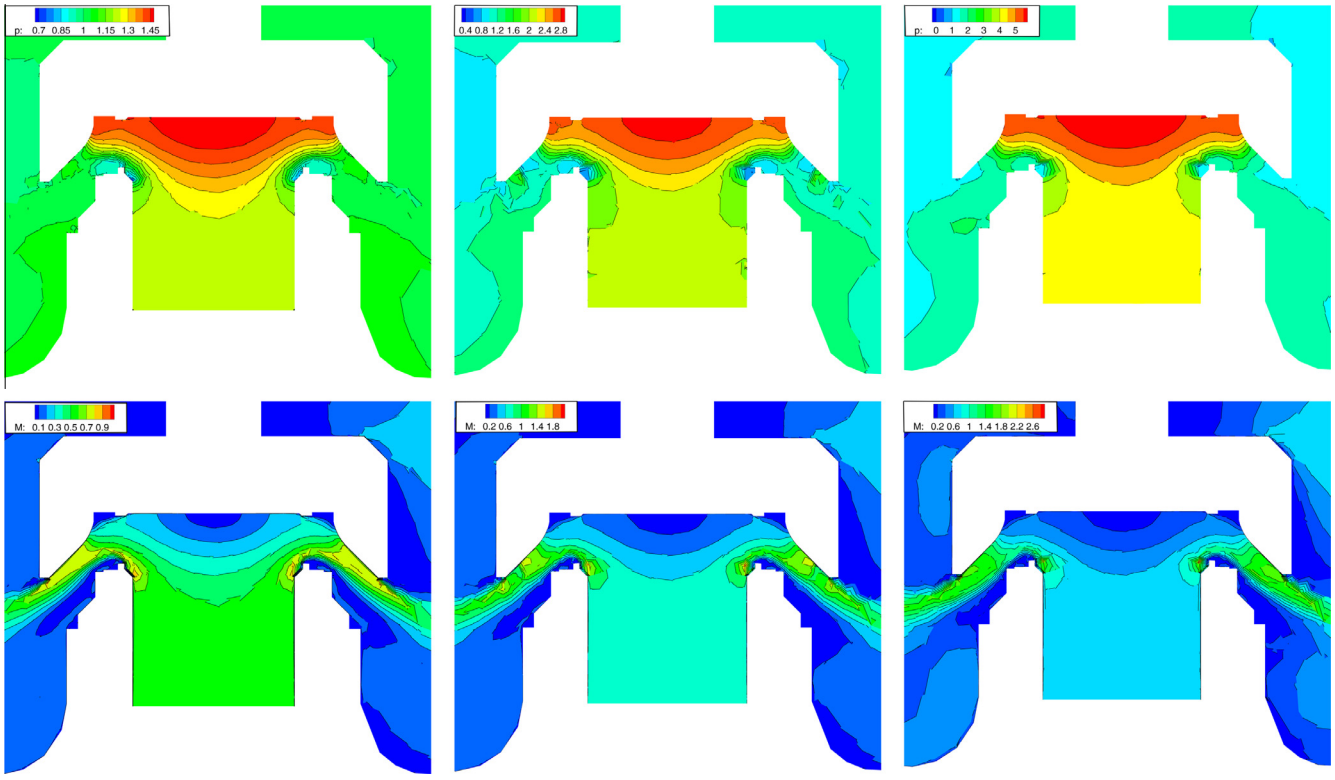

Fig. 7. $\mathbb{P}_1$ solution of valve operating with air at $\beta = 1.5,\ 3,\ 6$: detail of non-dimensional pressure and Mach number contours on the symmetry plane.

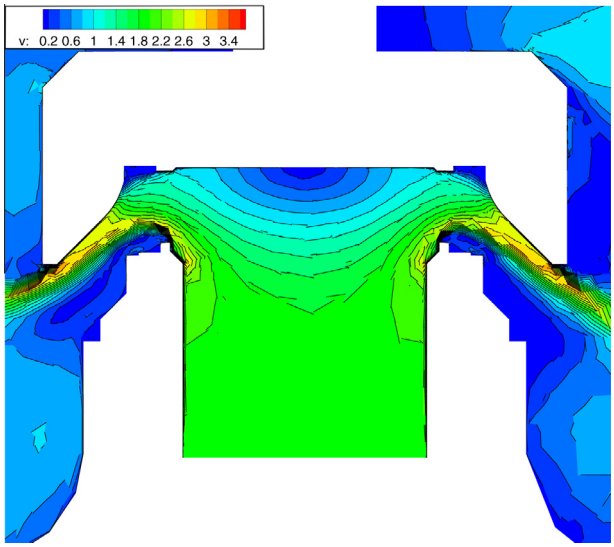

Fig. 8. $\mathbb{P}_1$ solution of valve operating with water at $\beta = 5.89$ at disc lift $h = 10$ mm: detail of non-dimensional velocity contours on the symmetry plane.

is the main responsible for the reduction in both discharge coefficient (from 0.76 down to about 0.6) and non-dimensional thrust (from 2.05–2.2 to 1.8–1.95). As a result, at the reduced lift, the thrust experienced in water at $\beta \simeq 6$ is now roughly 10% lower than the one occurring in air, instead of being 10% greater, *i.e.* the situation is reversed.

4. Concluding remarks

An accurate Discontinuous Galerkin solver for three-dimensional incompressible turbulent flows has been applied to investigate the different behavior of a safety relief valve when operating in water rather than in air. The code is based on the flux-compressibility approach originally described in [8,9] and here extended to three dimensional turbulent flows, with the implementation of the 2006 Wilcox k–ω turbulence model.

The code was first assessed on a 2″ J 3″ safety relief valve at $P_g \simeq 5$ bar for which experimental data were available. This test case is characterized by high flow velocities and strong viscous effects in a complex geometry. The computational mesh employed was quite coarse and also highly non-uniform close to solid walls due to the need of solving the k–ω equations down to the wall without using wall functions. This aspect stressed the code capabilities in terms of accuracy and robustness. Up to third-accurate ($\mathbb{P}_2$ polynomial approximation) numerical results confirm the quality of the proposed approach. However, future further study is foreseen to better understand the behavior of the incompressible solver also in comparison with the compressible one [1].

The incompressible and compressible DG codes have been used to highlight how and why the discharge coefficient and the force acting on the safety valve disc differ when operating with water or air. Notice that in the recent past it was normal practice among valve manufacturers to test the valve in air and then simply apply an empirical reduction factor to the discharge coefficient for the valve in water. This approach has been outdated by most recent reference standards (ISO and ASME) and nowadays tests both in air and water are required. The main observations resulting from the present investigation, performed at two disc lifts for pressure ratios varying from 1.5 to 6, are the following:

1. All incompressible solutions are similar and the different Reynolds numbers (in the range $1 \cdot 10^5$—$5 \cdot 10^5$) have a small influence.
2. The discharge coefficient in air is greater than in water and this is due to both positive compressibility effects and to the relevance of viscous losses only up to the sonic throat. Again, little advantage comes from a higher (about 2.5 times) Reynolds number in air.
3. In air, at full disc height (minimum flow area at inlet), K is greater and F is lower than at reduced lift. This is basically due to the outward sonic throat displacement.
4. In water, at full disc height, K and F are greater than at reduced lift owing to a more favorable flow path that reduces viscous losses.
5. As resulting from the above described trends, at full disc height, F_{water} is greater than F_{air} while at lower lift the situation is reversed.

The solution flow fields and the observations presented can be useful for valve designers, which must guarantee not only the correct opening and the rated mass flow at the prescribed pressure, but also the closing of the safety relief valve within a strict prescribed range. Targeting this aim when operating both with gases and liquids (*e.g.* steam and water) requires a careful definition of the safety valve trim. Furthermore, the computations are a necessary first step for the simulation of the actual unsteady opening–closing complete process which will be considered in a future work.

As a final comment, care must be exercised when extrapolating these results to different valve geometries and in any case a proper experimental and/or numerical testing procedure is advised.

References

[1] Dossena V, Marinoni F, Bassi F, Franchina N, Savini M. Numerical and experimental investigation on the performance of safety relief valves operating with different gases. J Pres Ves Pip 2013;104:21–9.

[2] Bassi F, Cecchi F, Franchina N, Rebay S, Savini M. High-order discontinuous Galerkin computation of axisymmetric transonic flows in safety relief valves. Comput Fluids 2011;49:203–13.

[3] Dossena V, Marinoni F, Di Vincenzo S, Boccazzi A. High pressure fluctuations induced by safety valves operating with liquids at very low lift. The American society of mechanical engineering. ASME PTC 25; 2004.

[4] Dossena V, Gaetani P, Marinoni F, Osnaghi C. On the influence of back pressure and size on the performance of safety valves. ASME paper PVP-1514. ASME; 2002.

[5] Gottlieb J, Groth CPT. Assessment of Riemann solvers for unsteady one-dimensional inviscid flows of perfect gases. J Comput Phys 1988;78:437–58.

[6] Bassi F, Rebay S, Mariotti G, Pedinotti S, Savini M. A high-order accurate discontinuous finite element method for inviscid and viscous turbomachinery flows. In: Decuypere R, Dibelius G, editors. 2nd European conference on turbomachinery fluid dynamics and thermodynamics. Antwerpen, Belgium: Technologisch Instituut; 1997. p. 99–108.

[7] Bassi F, Crivellini A, Rebay S, Savini M. Discontinuous Galerkin solution of the Reynolds-averaged Navier–Stokes and k–ω turbulence model equations. Comput Fluids 2005;34:507–40.

[8] Bassi F, Crivellini A, Pietro DAD, Rebay S. An artificial incompressibility flux for the discontinuous Galerkin solution of the incompressible Navier–Stokes equations. J Comput Phys 2006;218:794–815.

[9] Bassi F, Crivellini A, Pietro DD, Rebay S. An implicit high-order discontinuous Galerkin method for steady and unsteady incompressible flows. Comput Fluids 2007;36:1529–46.

[10] Wilcox DC. Turbulence modelling for CFD, 3rd ed. La Cañada, CA 91011, USA: DCW industries Inc.; 2006.

[11] Bassi F, Crivellini A, Rebay S, Savini M. Discontinuous Galerkin solution of the Reynolds averaged Navier–Stokes and k–ω turbulence model equations. Comput Fluids 2005;34:507–40.

[12] Bassi F, Crivellini A, Pietro DD, Rebay S. Very high-order accurate discontinuous Galerkin computations of transonic turbulent flows on aeronautical configurations. Notes Fluid Mech 2010;113:25–38.

[13] Arnold DN, Brezzi F, Cockburn B, Marini D. Unified analysis of discontinuous Galerkin methods for elliptic problems. SIAM J Numer Anal 2002;39(5):1749–79.

[14] Balay S, Brown J, Buschelman K, Gropp WD, Kaushik D, Knepley MG, et al. PETSc Web page; 2013. <http://www.mcs.anl.gov/petsc>.

[15] Balay S, Brown J, Buschelman K, Eijkhout V, Gropp WD, Kaushik D, et al. PETSc users manual. Tech. rep. ANL-95/11 - Revision 3.4. Argonne National Laboratory; 2013.

[16] Karypis G, Kumar V. METIS, a software package for partitioning unstructured graphs, partitioning meshes, and computing fill-reducing orderings of sparse matrices. Technical report version 4.0. University of Minnesota, Department of Computer Science/Army HPC Research Center; 1998.